

Quantum Simulation-Based Optimization of a Cooling System

Leonhard Hölscher^{1,2,3}*, Lukas Müller¹, Or Samimi⁴, and Tamuz Danzig⁴

¹*BMW Group, 80809 Munich, Germany*

²*Theoretical Physics, Saarland University, 66123 Saarbrücken, Germany*

³*Institute for Quantum Computing Analytics (PGI 12),*

Forschungszentrum Jülich, 52425 Jülich, Germany and

⁴*Classiq Technologies, 6473104 Tel Aviv-Yafo, Israel*

(Dated: July 9, 2025)

Engineering processes involve iterative design evaluations requiring numerous computationally intensive numerical simulations. Quantum algorithms promise up to exponential speedups for specific tasks relevant to numerical simulations. However, these advantages quickly vanish when considering data input and output on quantum computers. The recently introduced Quantum Simulation-Based Optimization (QuSO) algorithm circumvents this fundamental impediment by treating simulations as subproblems within a larger optimization problem. In this paper, we adapt and implement QuSO for a cooling system design problem. We validate the algorithm through statevector simulations and provide a detailed algorithmic complexity analysis indicating that the achievable speedup for this particular example is at most polynomial. Notably, we also specify the conditions under which QuSO could deliver exponential advantages. By providing this comprehensive demonstration, we highlight both the promise and practical constraints of QuSO in an engineering context, motivating further research into quantum algorithms for classical simulations and the search for suitable applications.

Keywords: Quantum Simulation-Based Optimization (QuSO); Quantum Approximate Optimization Algorithm (QAOA); Linear Combination of Unitaries (LCU); Quantum Singular Value Transform (QSVT); Quantum Amplitude Estimation (QAE)

I. INTRODUCTION

Numerical simulations of physical phenomena are highly relevant for industry and science. As models become more complex and accurate, the demand for computational resources increases steadily. Quantum computers are known for their potential to outperform ordinary computers in applications ranging from machine learning to optimization problems [1, 2]. Consequently, the question arises of whether quantum computers can also benefit the field of computer-aided engineering.

Numerous research papers on solving differential equations using quantum computers have appeared in recent years. These quantum approaches are based on analog quantum simulation [3], variational quantum algorithms (VQAs) [4–7], and fault-tolerant quantum algorithms [8–10]. The latter, in particular, allow a detailed algorithmic complexity analysis, revealing whether a quantum advantage exists. These fault-tolerant algorithms often rely on quantum linear system solvers [11–15] since solving a linear system of equations is a core step of many numerical simulation methods, such as the finite element method [16, 17].

However, the anticipated speedup of these quantum algorithms is often diminished by the algorithmic overhead associated with data input and output [18]. The recently proposed framework called Quantum Simulation-Based Optimization (QuSO) attempts to circumvent this limitation [19] by focusing not on the

simulation results, but rather on optimized parameters derived from simulations. This approach is known as simulation-based optimization [20, 21]. The optimization within QuSO can be efficiently addressed by well-known quantum optimization algorithms such as QAOA [22, 23]. Instead of constructing a cost Hamiltonian, QuSO implicitly evaluates the cost function through simulations, which typically involve solving at least one linear system of equations. Next to quantum linear system solvers and quantum optimization algorithms, this approach leverages quantum algorithms for block-encoding of matrices [2, 24–26] and amplitude estimation [27].

In this paper, we adapt QuSO to find the optimal configuration of connections within a cooling system. Despite our simplification of the cooling system, it is inspired by a real-world use case and thus of industrial relevance. A quantum algorithm for a similar problem has been studied in Ref. [28]. There, the authors wanted to find the optimal ground structure based on thermal material properties. Therefore, they also construct a VQA to optimize based on solving a linear system. However, they employ another VQA to solve the linear system. While the authors argue that their algorithm profits from the simultaneous evaluation of all possible ground structures, the variational nature of the algorithm does not allow an explicit statement about its complexity. Another quantum approach addressing a simulation-based optimization problem is presented in Ref. [29]. Based on quantum annealing, the authors solve a linear system to solve a topology optimization problem.

* leonhard.hoelscher@bmw.de

Since our implementation uses fault-tolerant subroutines, one of our significant contributions lies in giving a detailed complexity analysis for one iteration in an end-to-end algorithm for the cooling system application. In addition, we empirically study our adaption of QuSO by analyzing simulation results. The insights gained from this study will benefit future research on quantum algorithms for classical numerical simulations, as these methods can be adapted to other domains or extended to more realistic systems.

The remainder of the paper is organized as follows. Section II introduces the cooling system model and its formulation as a linear system of equations. In Section III, we detail our adaptation of QuSO, including all quantum subroutines and their algorithmic complexities, to encode the required matrix, solve the linear system, and transfer the result to the optimization algorithm. Section IV presents the results of our numerical simulations and analysis. Finally, Section V summarizes our findings, mentions potential improvements, and outlines directions for future research.

II. PROBLEM FORMULATION

A vehicle is composed of numerous complex components, ranging from mechanical systems like the drivetrain to electrical systems such as batteries and electric motors. These systems are interconnected, influencing one another, and must meet a wide range of requirements. For instance, depending on weather conditions, the battery may require heating or cooling while still providing sufficient power to the motor. Therefore, the components are connected by a cooling system with a cooling liquid, ensuring that all components have their desired temperature.

In this paper, we focus on simulating the vehicle's cooling system, as illustrated in Fig. 1 (a).

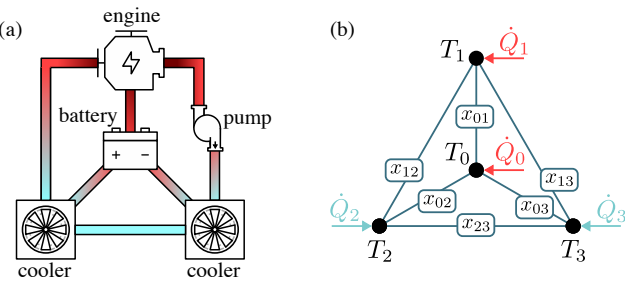


FIG. 1. Cooling system model. (a) Exemplary cooling system with an engine and battery as heat sources, two coolers, and a pump. (b) The simplification of the same cooling system that only covers heat conduction. x_{ij} is a binary variable defining if a connection exists between two nodes, T_i is the temperature at each node, and \dot{Q}_i is the heat transfer rate from either a heat or cooling source.

We apply several simplifications to define an initial quantum algorithm to address the problem. Heat

transfer generally occurs through convection, conduction, and radiation [30]. Given that convection is a highly nonlinear phenomenon and quantum operations are fundamentally linear, we omit this effect in our current approach for the sake of simplicity. While certain nonlinear problems can be addressed using linearization techniques on quantum computers [31–33], this lies beyond the scope of this work. Moreover, we do not consider the effects of radiation for now. This allows us to model the cooling system without a pump since we do not consider the motion of the cooling liquid. Instead, a system with N components or nodes is defined by thermal resistances R_{ij} of every connection between nodes i and j , and every heat or cooling source is defined by its external heat transfer rate \dot{Q}_i , as depicted in Fig. 1(b) for $N = 4$. In addition, we have binary variables

$$x = \{x_{ij}\}_{(i,j) \in \mathbf{E}} \quad (1)$$

defining if a connection between the two respective nodes exists. \mathbf{E} defines the set of m edges that we consider in our graph. If the graph is fully connected, we have

$$\mathbf{E} = \{(i,j) | 0 \leq i < j \leq N - 1\}. \quad (2)$$

Analogous to Ohm's law, Fourier's law of heat conduction in its simplest form is given by [30]

$$\dot{Q} = \frac{\Delta T}{R_{\text{th}}}, \quad (3)$$

where ΔT is the temperature difference between two nodes, and R_{th} is the corresponding thermal resistance. Energy conservation demands that the heat entering a node must equal the heat leaving it. This principle in combination with Eq. (3) leads to a linear system of equations

$$\mathbf{A}(x)\tilde{\mathbf{T}} = \mathbf{B}, \quad (4)$$

where $\mathbf{A}(x) \in \mathbb{R}^{N \times N}$, $\tilde{\mathbf{T}} \in \mathbb{R}^N$, and $\mathbf{B} \in \mathbb{R}^N$. The solution vector contains the temperatures at each node

$$\tilde{\mathbf{T}} = (\tilde{T}_0, \tilde{T}_1, \dots, \tilde{T}_{N-1})^T \quad (5)$$

with respect to the temperature T_{env} of the environment. Hence, $T_i = \tilde{T}_i + T_{\text{env}}$. The vector \mathbf{B} solely contains the external heat transfer rates

$$\mathbf{B} = (\dot{Q}_0, \dot{Q}_1, \dots, \dot{Q}_{N-1})^T. \quad (6)$$

Matrix $\mathbf{A}(x)$ is assembled as

$$\mathbf{A}(x) = \frac{1}{R_{\text{env}}} \mathbf{1} + \sum_{(i,j) \in \mathbf{E}} \frac{x_{ij}}{R_{ij}} \mathbf{U}_{ij}, \quad (7)$$

where \mathbf{U}_{ij} contains only four nonzero values:

$$\mathbf{U}_{ij} = \begin{pmatrix} & & & i & j \\ & \downarrow & & & \downarrow \\ & \vdots & & \vdots & \\ i \rightarrow & \cdots & 1 & \cdots & -1 & \cdots \\ & \downarrow & & & \downarrow & \\ & \vdots & & & \vdots & \\ j \rightarrow & \cdots & -1 & \cdots & 1 & \cdots \\ & \vdots & & & \vdots & \end{pmatrix}. \quad (8)$$

A detailed derivation of the linear system is given in Appendix A 1. Solving the linear system of Eq. (4) produces results consistent with those from steady-state simulations using engineering tools, such as Modelica-based software [34]. We demonstrate that in Appendix B.

III. QUANTUM SIMULATION-BASED OPTIMIZATION

In conventional simulation-based optimization [20, 21], the optimal system configuration is determined by iteratively simulating the system and adjusting its configuration based on the obtained simulation results. In our simple example of Fig. 1 (b), we are interested in the best system configuration x to achieve the lowest possible temperature at the battery T_0 , for example. Here, the computations are relatively inexpensive. This changes, however, for real-world systems with a vast design space where we need to consider dozens of components, different materials, and all relevant physical phenomena.

We can potentially reduce the computational workload by employing the quantum simulation-based optimization (QuSO) algorithm proposed in Ref. [19]. Therefore, we allow a superposition of configurations and thus their simultaneous evaluations using the Quantum Approximate Optimization Algorithm [22, 23]. For the simulation, we have the choice of various quantum linear system solvers. Within this work, we use the Quantum Singular Value transform (QSVT) [13, 14] to invert matrix \mathbf{A} and consequently solve the linear system in Eq. (4) by computing $\tilde{\mathbf{T}} = \mathbf{A}^{-1}\mathbf{B}$. The reduced runtime complexity of the QSVT algorithm results in another potential source of speedup for the simulation-based optimization procedure. To encode \mathbf{A} on the quantum computer, we apply the linear combination of unitaries (LCU) technique [26]. Once the temperatures are encoded in the amplitudes of a quantum state, we employ quantum amplitude estimation (QAE) [27] to extract the specific temperature of interest. This step is followed by quantum phase application (QPA), which maps the temperature into the phase as a cost term, thereby mimicking the action of a cost Hamiltonian.

Figure 7 illustrates the overall structure of the algorithm and its key quantum subroutines. In the

following, we briefly introduce each subroutine and its particular implementation to solve our QuSO problem of optimizing the simplified cooling system.

A. Quantum Approximate Optimization Algorithm

The Quantum Approximate Optimization Algorithm (QAOA) is designed to solve combinatorial optimization problems [22, 23]. It is inspired by the Adiabatic Theorem [35], which states that if a quantum system is initialized in the ground state of a certain initial Hamiltonian and evolves slowly enough under a time-dependent Hamiltonian, the system will remain in its instantaneous ground state, eventually reaching the ground state of the Hamiltonian of interest. Instead of continuous evolution, QAOA implements a discrete, gate-based approach. The algorithm begins by initializing all qubits to the $|+\rangle$ state, representing the ground state of the mixer Hamiltonian

$$H_M = \sum_{i=0}^{m-1} -X_i, \quad (9)$$

where X_i is the Pauli-X operator applied to the i -th qubit. The optimization problem is encoded in the cost Hamiltonian H_C . By alternately applying p layers of the time evolutions $U_C(\gamma) = e^{-i\gamma H_C}$ and $U_M(\beta) = e^{-i\beta H_M}$, QAOA corresponds to a Suzuki-Trotter approximation [36, 37] of the adiabatic evolution. For each layer, the parameters γ and β are classically updated to minimize the expectation value $\langle H_C \rangle$, which acts as a cost function. The circuit structure of QAOA is briefly illustrated in Fig. 2.

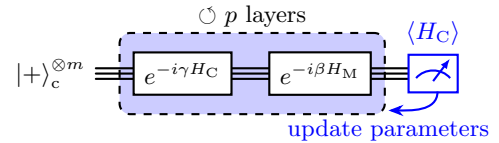


FIG. 2. QAOA circuit with variational parameters γ , β and Hamiltonians H_C and H_M . The blue section highlights a single QAOA layer which is repeated p times with individual parameters. A final measurement of $\langle H_C \rangle$ is used to classically optimize γ and β . After several iterations of that procedure, the circuit prepares the desired ground state of H_C .

To solve a QuSO problem, however, we need to perform a simulation to compute the cost function. Hence, we build a quantum algorithm to implement the cost layer as

$$U_C(\gamma) |x\rangle_c = e^{-i\gamma c(x)} |x\rangle. \quad (10)$$

Here, $c(x)$ is the cost associated with the simulation for the configuration x . This can be interpreted as a time evolution under the cost Hamiltonian

$$H_C = \sum_{x=0}^{2^m-1} c(x) |x\rangle\langle x|_c. \quad (11)$$

Throughout the remainder of this paper, the QAOA register storing the configuration is referred to as the c-register.

B. Matrix Block-Encoding

To build the cost layer of Eq. (10), we need to compute the cost $c(x)$ on the quantum computer based on the solution of the linear system in Eq. (4). Therefore, we encode the respective matrix $\mathbf{A}(x)$ in the upper left block of a unitary operator

$$U_{\mathbf{A}} = \begin{pmatrix} \mathbf{A}(x) & * \\ * & * \end{pmatrix}. \quad (12)$$

Notably, $\mathbf{A}(x)$ depends on the configuration x , which is stored in the c-register as $|x\rangle_c$. If several configurations exist in superposition, we also need to prepare our matrix in superposition.

We achieve that block-encoding using the technique of Linear Combination of Unitaries (LCU) [26]. As one can deduce from the name LCU, $\mathbf{A}(x)$ is considered as a linear combination of unitary operators U_k :

$$\mathbf{A}(x) = \sum_k \lambda_k U_k \quad \text{with} \quad \lambda_k > 0. \quad (13)$$

Therefore, the operation V prepares an auxiliary register ℓ to

$$V |0\rangle_\ell |\psi\rangle_d = C_\ell \sum_k \sqrt{\lambda_k} |k\rangle_\ell |\psi\rangle_d, \quad (14)$$

where $C_\ell = (\sum_k \lambda_k)^{-1/2}$ ensures normalization. The state preparation step is followed by an operation M_U which consists of a series of multicontrolled unitaries U_k such that each coefficient $\sqrt{\lambda_k}$ is in front of U_k :

$$M_U V |0\rangle_\ell |\psi\rangle_d = C_\ell \sum_k |k\rangle_\ell \sqrt{\lambda_k} U_k |\psi\rangle_d. \quad (15)$$

Finally, we only have to unprepare the auxiliary register to obtain

$$\underbrace{V^\dagger M_U V}_{=U_{\text{LCU}}} |0\rangle_\ell |\psi\rangle_d = C_\ell^2 |0\rangle_\ell \underbrace{\sum_k \lambda_k U_k}_{=\mathbf{A}(x)} |\psi\rangle_d + |\dots\rangle. \quad (16)$$

Consequently, if we only consider the state in the d-register associated with $|0\rangle_\ell$, we indeed apply the matrix $\mathbf{A}(x)$ to the $|\psi\rangle_d$ state. All other terms in Eq. (16) are irrelevant and thus not further specified. If one is only interested in a state proportional to $\mathbf{A}(x) |\psi\rangle_d$, one could add a postselection measurement step, such that the auxiliary register collapses to $|0\rangle_\ell$. In our case, we omit the measurement as we require a coherent operation.

If we compare Eq. (13) with the definition of $\mathbf{A}(x)$ in Eq. (7), the LCU construction becomes clear. We can identify the coefficients λ_k as either $(2R_{\text{env}})^{-1}$ or x_{ij}/R_{ij}

and the unitaries U_k as $\mathbb{1}$ or $[\mathbf{U}_{ij}/2]_{\text{block}}$. The latter is the block-encoding of the matrix $\mathbf{U}_{ij}/2$ in Eq. (8), and the factor of $1/2$ ensures proportionality.

While the implementation of $\mathbb{1}$ is straightforward, we explain the construction of $[\mathbf{U}_{ij}/2]_{\text{block}}$ in the following. Central to this construction is the LCU of

$$\frac{1}{2}\mathbb{1} - \frac{1}{2}X = \frac{1}{2} \begin{pmatrix} 1 & -1 \\ -1 & 1 \end{pmatrix}, \quad (17)$$

which acts on a single qubit and requires an auxiliary qubit initialized in an equal superposition state via a Hadamard gate ($V = H$).

We first embed this 2×2 matrix into the upper-left block of an $N \times N$ zero-padded matrix, effectively constructing $[\mathbf{U}_{01}/2]_{\text{block}}$. To achieve this, we introduce a flag qubit f and an operation F , which flips f whenever all but the least significant qubit of $|\psi\rangle_d$ are not in the $|0\rangle$ state. By treating f as an auxiliary qubit of the block-encoding, the values outside the 2×2 block are shifted out of the upper-left corner. The resulting circuit is shown in Fig. 3 for $N = 8$.

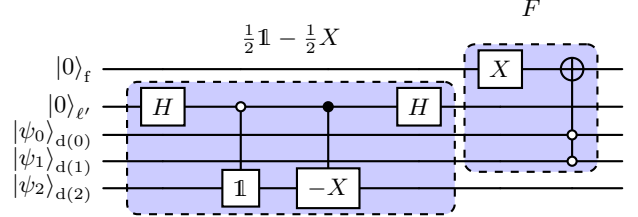


FIG. 3. Quantum circuit to embed the LCU of Eq. (17) in the upper left block of an 8×8 zero-padded matrix. This corresponds to $[\mathbf{U}_{01}/2]_{\text{block}}$, and $d(2)$ represents the least significant qubit.

To generalize this to arbitrary indices i and j , we permute the basis states such that

$$\begin{aligned} |i\rangle_d &= |i_0 i_1 \dots i_{n-1}\rangle \mapsto |0\rangle = |00 \dots 0\rangle \\ |j\rangle_d &= |j_0 j_1 \dots j_{n-1}\rangle \mapsto |1\rangle = |00 \dots 1\rangle, \end{aligned} \quad (18)$$

where $n = \lceil \log_2 N \rceil$. This is achieved by first applying X gates on the qubits where the binary representation of i has a 1, resulting in $|i\rangle \mapsto |0\rangle$ and $|j\rangle \mapsto |j \oplus i\rangle$. We then use CNOT gates controlled on a qubit corresponding to a 1 in the binary representation of $j \oplus i$ applied on the remaining 1's. A final SWAP operation moves the qubit with the remaining 1 to the least significant position, meaning $|j\rangle \mapsto |1\rangle$. We term the entire permutation in Eq. (18) P_{ij} .

The block-encoding of $\mathbf{U}_{ij}/2$ is thus given by

$$\left[\frac{1}{2} \mathbf{U}_{ij} \right]_{\text{block}} = P_{ij}^\dagger F \left[\frac{1}{2} \mathbb{1} - \frac{1}{2} X \right]_{\text{LCU}} P_{ij}, \quad (19)$$

where the subscript LCU indicates that the expression is implemented with the LCU method.

The worst-case scenario for the implementation of the P_{ij} operation in terms of gate depth occurs when

$i = (11\dots1)_2$ and $j = (00\dots0)_2$. This case requires $\lceil \log_2 N \rceil X$ gates, $\lceil \log_2 N \rceil - 1$ CNOT gates, and one SWAP gate. Consequently, the algorithmic complexity of block-endoding $\mathbf{U}_{ij}/2$ in Eq. (19) is $\mathcal{O}(\log N)$. The entire LCU-based construction of $\mathbf{A}(x)$ is given by

$$U_{\mathbf{A}} = \left[\frac{C_{\ell}}{2R_{\text{env}}} \mathbb{1} + C_{\ell} \sum_{(i,j) \in \mathbf{E}} \frac{x_{ij}}{R_{ij}} \left[\frac{1}{2} \mathbf{U}_{ij} \right]_{\text{block}} \right]_{\text{LCU}}, \quad (20)$$

which comprises $m + 1$ terms. Preparing these $m + 1$ amplitudes typically requires $\mathcal{O}(m)$ operations [38–41]. Additionally, there are m controlled unitaries, resulting in an overall gate complexity for $U_{\mathbf{A}}$ of

$$\mathcal{G}_{\text{LCU}} = \mathcal{O}(m \log N). \quad (21)$$

As some coefficients in Eq. 20 explicitly depend on the binary variables x_{ij} and therefore on the configuration x , we add controls on the c-register. Consequently, if multiple configurations exist in superposition, the resulting circuit achieves a coherent encoding of $\mathbf{A}(x)$ in superposition. The corresponding quantum circuit is shown in Fig. 4.

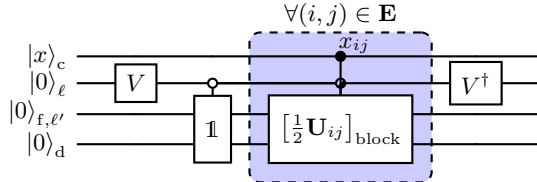


FIG. 4. Quantum circuit for the LCU-based block-endoding of $\mathbf{A}(x)$ (cf. Eq. (20)). The block-endoding of $\mathbf{U}_{ij}/2$ is not only controlled on the ℓ -register (indicated by the half-filled control node) but also on the respective qubit $|x_{ij}\rangle$ of the c-register. The operation within the blue shaded area is repeated for all connections $(i,j) \in \mathbf{E}$.

For a graph with N nodes, the number of edges m in a connected graph is bounded by $N - 1 \leq m \leq N(N - 1)/2$. In practice, we anticipate sparse graphs for realistic systems involving dozens of components. Given that the maximum number of pipes that can be connected to a node is physically constrained, we assume a finite maximum degree of the graph $d_{\text{max}} = \mathcal{O}(1)$. This leads to an upper bound of

$$m = \frac{1}{2} \sum_{i=0}^{N-1} d_i \leq \frac{1}{2} N d_{\text{max}}, \quad (22)$$

where d_i represents the degree of node i . Using this sparsity condition, we express the gate complexity in Eq. (21) in terms of N as

$$\mathcal{G}_{\text{LCU}} = \mathcal{O}(N \log N). \quad (23)$$

The whole matrix construction requires $\lceil \log_2(m + 1) \rceil$ auxiliary qubits in the ℓ -register for the outer LCU layer,

one ℓ' qubit for the inner LCU layer, one f qubit, and $\lceil \log_2 N \rceil$ qubits for the data register d .

Due to the normalization condition and the LCU procedure, the resulting block-encoded matrix corresponds to $C_{\ell}^2 \mathbf{A}(x)/2$.

C. Quantum Singular Value Transform

The Quantum Singular Value Transform (QSVT) is a quantum algorithm that manipulates the singular values of a matrix encoded within a quantum circuit [13, 14]. By doing so, it is capable of solving similar problems such as Quantum Phase Estimation (QPE) [42], Grover's search [43], Hamiltonian simulation [44], and matrix inversion [14]. The algorithm applies a polynomial transformation on the singular values $P^{\text{sv}}(\mathbf{A})$ of matrix $\mathbf{A} = \mathbf{W}_{\Sigma} \mathbf{\Sigma} \mathbf{V}_{\Sigma}^{\dagger}$, where $\mathbf{\Sigma}$ contains the singular values in its diagonal. For our square matrix, the QSVT operator is defined as

$$U_{\phi} = \begin{cases} \prod_{k=1}^{d-1/2} \Pi_{\phi_{2k}} U_{\mathbf{A}}^{\dagger} \Pi_{\phi_{2k+1}} U_{\mathbf{A}}, & \text{for odd } d \\ \prod_{k=1}^{d/2} \Pi_{\phi_{2k-1}} U_{\mathbf{A}}^{\dagger} \Pi_{\phi_{2k}} U_{\mathbf{A}}, & \text{for even } d \end{cases} = \begin{pmatrix} P^{\text{sv}}(\mathbf{A}) & * & * \\ * & * & * \end{pmatrix}. \quad (24)$$

Here, $U_{\mathbf{A}}$ is the block-endoding of $\mathbf{A}(x)$ as defined in Eq. (20), and Π_{ϕ_i} is a projector-controlled phase-shift operation given by $\Pi_{\phi_i} = e^{i\phi_i(2\pi-1)}$, where $\Pi = |0\rangle\langle 0|_{\ell,f,e'}$ is the projector associated with our block-endoding [45]. The corresponding quantum circuit in Fig. 5 illustrates how Π_{ϕ_i} can be constructed using an auxiliary qubit, two CNOT gates, and a Z phase gate.

Within the QuSO algorithm, we employ the QSVT routine to invert $\mathbf{A}(x)$, thereby solving the linear system in Eq. (4). Therefore, we choose the phase angles $\phi = (\phi_1, \phi_2, \dots, \phi_d)$ such that the resulting polynomial approximates the reciprocal function $P_{\text{inv}}(x_p) \approx C_p/x_p$, where C_p ensures that the function values lie within $[-1, 1]$ [13, 14, 46]. In combination with the block-endoding of \mathbf{A}^{\dagger} , the resulting operator approximately block-endodes \mathbf{A}^{-1} up to a constant factor:

$$\begin{aligned} P_{\text{inv}}^{\text{sv}}(\mathbf{A}^{\dagger}) &= \mathbf{V}_{\Sigma} P_{\text{inv}}(\mathbf{\Sigma}) \mathbf{W}_{\Sigma}^{\dagger} \\ &\approx C_p \mathbf{V}_{\Sigma} \mathbf{\Sigma}^{-1} \mathbf{W}_{\Sigma}^{\dagger} = \frac{2}{C_{\ell}^2} C_p \mathbf{A}^{-1}. \end{aligned} \quad (25)$$

To implement this inversion, we use the *matrix-inversion polynomial* $P_{\epsilon,\mu}^{\text{MI}}(x_p)$ introduced in Ref. [14]. This polynomial is an $\epsilon\mu/2$ -close approximation to $(\mu/2)/x_p$ for $x_p \in [-1, 1] \setminus [-\mu, \mu]$. Thus, $C_p = \mu/2$, where μ is the threshold value corresponding to the smallest invertible singular value and thus satisfies $\mu \leq \sigma_{\min} C_{\ell}^2/2 \leq 1/\kappa$ [47], and ϵ controls the accuracy. Here, σ_{\min} denotes the smallest singular value of $\mathbf{A}(x)$, and κ is its condition

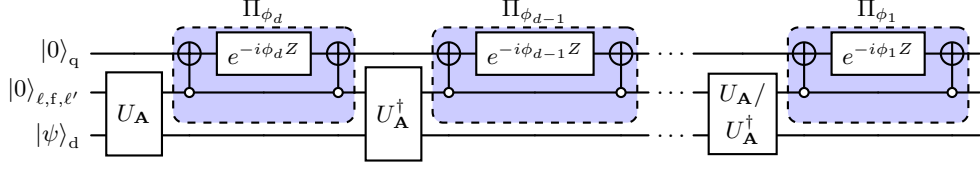


FIG. 5. Quantum circuit representation of the Quantum Singular Value Transformation (QSVT) operator. The unitary U_A denotes the block-encoding of the matrix \mathbf{A} , and the blue-shaded areas represent projector-controlled phase-shift operators. For even values of d , the rightmost block-encoding operator U_A should be replaced with its Hermitian adjoint U_A^\dagger . To improve readability, we have omitted the controls on the c-register.

number. The polynomial has odd parity and its degree scales as $\mathcal{O}(\kappa \log(\kappa/\epsilon))$, resulting in a similar number of calls to the block-encoding U_A . Since we know the exact structure of $\mathbf{A}(x)$ for all configurations x , we can derive an asymptotic scaling of $\kappa = \mathcal{O}(R_{\text{env}}/R_{\min})$, where R_{\min} is the minimum thermal resistance of the system. A detailed derivation can be found in Appendix A 2. Consequently, the QSVT circuit has a gate complexity of

$$\mathcal{G}_{\text{QSVT}} = \mathcal{O}\left(\frac{R_{\text{env}}}{R_{\min}} \log\left(\frac{R_{\text{env}}}{\epsilon R_{\min}}\right)\right) \times \mathcal{G}_{\text{LCU}}. \quad (26)$$

In order to obtain the temperature vector $\tilde{\mathbf{T}} = \mathbf{A}^{-1}\mathbf{B}$, we need to prepare \mathbf{B} in the data register prior to applying the QSVT operator:

$$V_B |0\rangle = C_B \sum_{k=0}^{N-1} \dot{Q}_k |k\rangle. \quad (27)$$

Here, $C_B = (\sum_k \dot{Q}_k^2)^{-1/2}$ ensures normalization. In realistic systems, the number of external heat and cooling sources N_Q is much smaller than N , as not every component produces heat or actively cools the system. As a result, the vector \mathbf{B} is sparse, containing only N_Q nonzero values. This sparsity reduces the gate complexity for the state preparation operation V_B from $\mathcal{O}(N)$ to $\mathcal{O}(N_Q \log N)$ [2, 48]. Since \mathcal{G}_{LCU} in Eq. (23) dominates, the overall gate complexity of the linear system solving routine $L = U_\phi V_B$ remains equivalent to $\mathcal{G}_{\text{QSVT}}$ in Eq. (26).

After applying L , we obtain a state proportional to $\tilde{\mathbf{T}}$:

$$\begin{aligned} L |0\rangle_{q,\ell,f,\ell'} |0\rangle_d &= U_\phi \left(|0\rangle_{q,\ell,f,\ell'} V_B |0\rangle_d \right) \\ &= \frac{2}{C_\ell^2} C_p C_B |0\rangle_{q,\ell,f,\ell'} \underbrace{\sum_{k=0}^{N-1} \tilde{T}_k |k\rangle_d}_{=\tilde{\mathbf{T}}} + |\dots\rangle. \end{aligned} \quad (28)$$

D. Quantum Amplitude Estimation

As the name Quantum Amplitude Estimation (QAE) [27] suggests, it is an algorithm to extract the absolute value of a quantum amplitude a of some state

$$|\phi\rangle = a |\alpha\rangle + \sqrt{1-a^2} |\alpha^\perp\rangle. \quad (29)$$

Therefore, it uses Quantum Phase Estimation (QPE) [42] (cf. Fig. 6) with the Grover operator

$$G = -LS_0L^\dagger S_\alpha, \quad (30)$$

where L prepares the solution of the linear system, $S_0 = \mathbb{1} - 2|0\rangle\langle 0|$ performs a reflection about the $|0\rangle$ state, and $S_\alpha = \mathbb{1} - 2|\alpha\rangle\langle\alpha|$ reflects about the $|\alpha\rangle$ state.

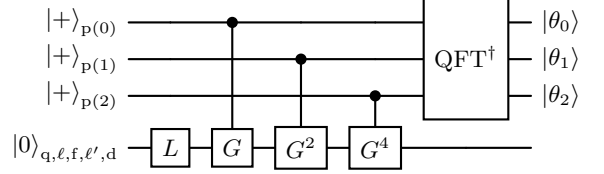


FIG. 6. Quantum circuit for quantum amplitude estimation without measurements. To improve readability, we have omitted the controls on the c-register.

In the subspace spanned by $|\alpha\rangle$ and $|\alpha^\perp\rangle$, the Grover operator has two eigenstates

$$|\psi_\pm\rangle = \frac{1}{\sqrt{2}}(|\alpha\rangle \pm i|\alpha^\perp\rangle) \quad (31)$$

with the corresponding eigenvalues

$$\lambda_\pm = e^{\pm i2\pi\theta}, \quad (32)$$

where the phase θ is related to the amplitude a by

$$|a| = \sin(\pi\theta). \quad (33)$$

At the end of the QAE circuit, the phase register p , consisting of k qubits, encodes the binary fraction of $\theta = (0.\theta_0\theta_1\dots\theta_{k-1})_2$. The precision of θ is determined by the error $\delta = 2^{-k}$, resulting in a gate complexity for QAE of

$$\mathcal{G}_{\text{QAE}} = \mathcal{O}\left(\frac{1}{\delta}\right) \times \mathcal{G}_{\text{QSVT}}. \quad (34)$$

In our QuSO algorithm, we compute the temperature vector $\tilde{\mathbf{T}}$ in the data register d , where all auxiliary qubits are in the $|0\rangle$ state. We employ QAE to extract the temperature of interest \tilde{T}_α , which corresponds to the cost function we aim to minimize. Within this work, we

assume that $\tilde{T}_\alpha > 0$ to avoid the need for representing negative numbers with binary fractions. If this condition is not met, two's complement can be used instead [19]. At the end, the phase is given by

$$\theta = \arcsin\left(2C_p C_B \tilde{T}_\alpha / C_\ell^2\right) / \pi. \quad (35)$$

E. Quantum Phase Application

The phase register p encodes the phase θ from Eq.(35). The Quantum Phase Application (QPA) routine performs

$$\text{QPA}(\gamma) |\theta\rangle_p = e^{-i\gamma f(\theta)} |\theta\rangle_p, \quad (36)$$

where $f(\theta) = \sin(\pi\theta)$ such that we obtain the cost layer of Eq.(10) with $c(x) = \tilde{T}_\alpha \cdot 2C_p C_B / C_\ell^2$. For a phase register of size k , $f(\theta)$ can be implemented exactly by constructing a polynomial of degree up to 2^k that matches $f(\theta)$ at all 2^k discrete inputs [49]. The polynomial is realized using Pauli-Z operators

$$\begin{aligned} \text{QPA}(\gamma) |\theta\rangle_p &= e^{-i\gamma \sum_{S \subseteq \{0,1,\dots,k-1\}} a_S \otimes_{i \in S} Z_i} \\ &= \prod_{S \subseteq \{0,1,\dots,k-1\}} e^{-i\gamma a_S \otimes_{i \in S} Z_i}, \end{aligned} \quad (37)$$

where a_S are the 2^k polynomial coefficients. The optimal implementation of $\text{QPA}(\gamma)$ requires

$$\mathcal{G}_{\text{QPA}} = \mathcal{O}(2^k) = \mathcal{O}\left(\frac{1}{\delta}\right) \quad (38)$$

gates [50].

Since the sine function can be well-approximated using low-degree polynomials, the number of gates in Eq.(37) can be significantly reduced. However, as \mathcal{G}_{QAE} is typically the dominant cost, implementing an exact QPA circuit becomes negligible in the overall complexity.

F. QuSO Algorithm

In the previous sections, we introduced the vanilla QAOA algorithm for combinatorial optimization problems, outlined the encoding of matrix $\mathbf{A}(x)$ using nested LCU block-encodings, and described the use of QSVT to invert $\mathbf{A}(x)$ and solve the linear system in Eq.(4). We further detailed the extraction of a single amplitude \tilde{T}_α from the solution vector $\tilde{\mathbf{T}}$ via QAE, as well as the application of this amplitude as a global phase using QPA to implement the cost layer of the QAOA algorithm $U_C(\gamma)$ from Eq.(10). The QuSO algorithm integrates all these quantum subroutines into a complete QAOA-based framework to find the optimal

configuration of the system [19]. The overall QuSO circuit is depicted in Fig. 7.

The cost layer $U_C(\gamma)$ consists of QAE, followed by QPA, and concludes with QAE^\dagger to disentangle the auxiliary qubits

$$U_C(\gamma) = \text{QAE}^\dagger \text{QPA}(\gamma) \text{QAE}. \quad (39)$$

The QAE routine introduced here corresponds to the QSim subroutine described in Ref. [19], with the difference that our implementation computes the phase

$$\theta = \arcsin(c(x)) / \pi \quad (40)$$

instead of the cost $c(x)$. Ideally, the k qubits in the p -register are sufficient to represent θ exactly, and the auxiliary qubits (registers p , q , ℓ , f , ℓ' , and d) are uncomputed to the $|0\rangle$ state after each cost layer. In general, however, k might be insufficient, so the phases θ are computed with an error of $\delta = 2^{-k}$, and the auxiliary qubits are not perfectly reset. The resulting error scales as $\mathcal{O}(\delta)$ and is thus negligible for small δ . Further details are provided in Appendix C.

After applying the p cost and mixer layers, the optimal configuration can be extracted by sampling from the c -register, identifying the bitstring with the highest probability. This bitstring corresponds to the current best configuration of the system. For classical optimization, the cost of the identified configuration must also be evaluated, which can be achieved with an additional QAE execution and a subsequent measurement of the phase register. An additional curve fit further increases the accuracy of the cost [51].

The gate complexity of a single iteration of QuSO is derived by aggregating the complexities of its quantum subroutines. Table I provides an overview of all complexities.

Although the current form of the QuSO algorithm optimizes only for the minimal temperature at a single node, it can be extended to accommodate more sophisticated cost functions. These may involve combining temperatures across multiple nodes or incorporating additional cost Hamiltonians. Furthermore, the algorithm's flexibility allows to consider additional constraints by modifying the mixer layer $U_M(\beta)$ [23, 52].

IV. NUMERICAL EXPERIMENTS

To evaluate the performance of QuSO, we implemented it for the cooling system use case. The corresponding code is available in Refs. [53, 54].

A. QSVT for Cooling System Simulation

In our first simulation, we run the QSVT-based linear system solver L from Eq.(28) to evaluate the battery

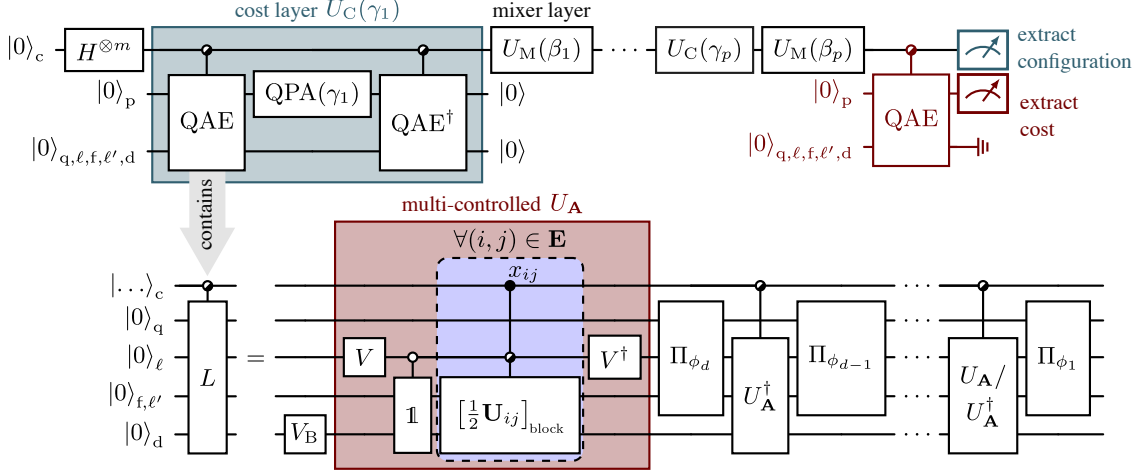


FIG. 7. Overview of the QuSO circuit. The upper part shows the QAOA circuit, starting with Hadamard gates and alternating cost and mixer layers. Each cost layer includes QAE to extract the cost into the phase register p , $QPA(\gamma)$ to apply it as a phase, and QAE^\dagger to disentangle auxiliary qubits. The c-register is measured to extract the optimal bitstring, and an additional QAE run retrieves its associated cost. The lower part illustrates the quantum linear system solver L , comprising state preparation V_B for encoding B and QSVT for inverting A . Nested LCUs in the block-encoding U_A have controls on $|x_{ij}\rangle$ states in the c-register, ensuring inclusion only for valid terms. Half-filled control nodes represent one or more multi-controlled operations.

Algorithm	Gate Complexity \mathcal{G}	Space Complexity \mathcal{S}	Required Qubits \mathcal{N}
LCU	$\mathcal{O}(N \log N)$	$\mathcal{O}(\log N)$	$\lceil \log_2(m+1) \rceil + \lceil \log_2 N \rceil + 2$
QSVT	$\mathcal{O}\left(\frac{R_{\text{env}}}{R_{\min}} \log\left(\frac{R_{\text{env}}}{\epsilon R_{\min}}\right)\right) \times \mathcal{G}_{\text{LCU}}$	$\mathcal{S}_{\text{LCU}} + \mathcal{O}(1)$	$\mathcal{N}_{\text{LCU}} + 1$
QAE	$\mathcal{O}\left(\frac{1}{\delta}\right) \times \mathcal{G}_{\text{QSVT}}$	$\mathcal{S}_{\text{QSVT}} + \mathcal{O}\left(\log \frac{1}{\delta}\right)$	$\mathcal{N}_{\text{QSVT}} + \lceil \log_2 \frac{1}{\delta} \rceil$
QPA	$\mathcal{O}\left(\frac{1}{\delta}\right)$	$\mathcal{O}\left(\log \frac{1}{\delta}\right)$	$\lceil \log_2 \frac{1}{\delta} \rceil$
QuSO	$\mathcal{O}\left(N \log N \frac{R_{\text{env}}}{\delta R_{\min}} \log\left(\frac{R_{\text{env}}}{\epsilon R_{\min}}\right)\right)$	$\mathcal{O}\left(\max\{N, \log \frac{1}{\delta}\}\right)$	$m + \lceil \log_2(m+1) \rceil + \lceil \log_2 N \rceil + \lceil \log_2 \frac{1}{\delta} \rceil + 3$

TABLE I. Gate and space complexities, as well as total qubit counts for QuSO and its subroutines.

temperature \tilde{T}_0 . Accordingly, the cost function is defined as

$$c(x) = \tilde{T}_0 \cdot 2C_p C_B / C_\ell^2. \quad (41)$$

The system parameters used in our simulations are listed in Table II.

$$\begin{aligned} R_{01} &= 5 \text{ mK W}^{-1} & \dot{Q}_0 &= 2 \text{ kW} & R_{\text{env}} &= 10 \text{ mK W}^{-1} \\ R_{02} = R_{03} &= 6 \text{ mK W}^{-1} & \dot{Q}_1 &= 4 \text{ kW} & T_{\text{env}} &= 293 \text{ K} \\ R_{12} = R_{13} &= 7 \text{ mK W}^{-1} & \dot{Q}_2 &= -0.2 \text{ kW} \\ R_{23} &= 8 \text{ mK W}^{-1} & \dot{Q}_3 &= -2 \text{ kW} \end{aligned}$$

TABLE II. System parameters used for our simulations.

The thermal resistances were chosen to have a realistic order of magnitude and to satisfy $R_{\text{env}} > R_{\min}$, reflecting the expectation that less heat is transferred to the environment than through dedicated connections within the cooling system. At the same time, we tuned the ratio R_{env}/R_{\min} such that the smallest singular value $\sigma_{\min} = 0.05$ remains manageable.

We employ the LCU block-encoding U_A (cf. Eq. (20)) together with QSVT, utilizing the polynomial mentioned in section III C. Its accuracy is set by the parameters μ and ϵ . We ran simulations with μ ranging from $1/38$ to $1/2$, and ϵ ranging from 1×10^{-3} to 1×10^{-1} . In order to compare the resulting cost $c(x)$ for all 64 configurations x , we normalized the cost as

$$\tilde{c}(x) = \frac{c(x)}{\max_x c(x)} \quad (42)$$

since the scaling factor C_p varies for different μ and ϵ . Fig. 8(a) shows the normalized cost $\tilde{c}(x)$ for several μ , $\epsilon = 1 \times 10^{-1}$, and all configurations x . As expected, smaller values of μ yield QSVT results that are closer to the target values $\tilde{c}_{\text{target}}$. This trend is illustrated in Fig. 8(b), where the distance

$$\Delta = |\tilde{c}_{\text{target}} - \tilde{c}| \quad (43)$$

is plotted against μ for different values of ϵ . Once μ is sufficiently small to resolve the smallest singular

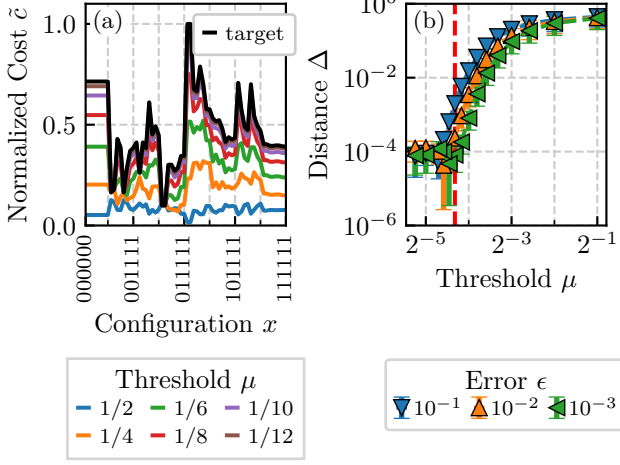


FIG. 8. Simulation results for the linear system solver L , which incorporates the LCU block-encoding U_A from Eq. (20) and QSVT. Panel (a) presents the normalized cost \tilde{c} for each configuration x at various errors ϵ . Panel (b) illustrates how the distance Δ (cf. Eq. (43)) decreases with threshold μ and error ϵ ; here, the mean error is shown with standard deviation error bars.

value σ_{\min} , QSVT successfully inverts the block-encoded matrix. Consequently, no further improvement is observed for $\mu < \sigma_{\min}$.

B. QuSO for Cooling System Optimization

Having verified that our cooling system simulation using QSVT yields correct results, we now evaluate the complete QuSO algorithm. However, the entire circuit, including the auxiliary qubit registers and all subroutines within QAE, becomes computationally intensive and thus infeasible to simulate with our available hardware. To address this challenge, we employ two shortcuts only possible in statevector simulation.

First, we precompute the costs $c(x)$ classically for all configurations x , thereby creating a lookup table. Using this precomputed data, we define a dummy state

$$|\phi(x)\rangle_d = c(x)|0\rangle_d + \sqrt{1 - c(x)^2}|1\rangle_d. \quad (44)$$

Now, instead of using QAE to estimate $c(x)$, we directly prepare the theoretical outcome of QAE [42] to this dummy state as

$$V_\psi|0\rangle_p|0\rangle_d = -\frac{i}{\sqrt{2}} \sum_{j=0}^{2^k-1} e^{-i\pi\theta} \alpha_+(j) |j\rangle_p |\psi_+\rangle_d - e^{i\pi\theta} \alpha_-(j) |j\rangle_p |\psi_-\rangle_d, \quad (45)$$

where $|\psi_\pm\rangle$ are given by Eq. (31), θ is given by Eq. (40),

and $\alpha_\pm(j)$ are the QPE amplitudes given by

$$\alpha_\pm(j) = \frac{1}{2^k} \sum_{l=0}^{2^k-1} e^{-i2\pi l(2^{-k}j \mp \theta)}. \quad (46)$$

Thus, we replace the QAE and QAE^\dagger routines in Eq. (39) with individual state preparations V_ψ that are controlled on the c-register for every configuration x , as illustrated in Fig. 9.

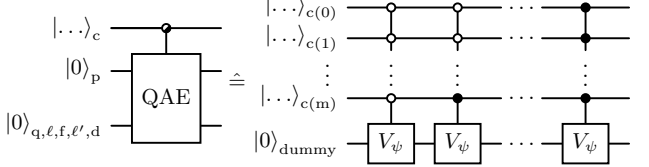


FIG. 9. Replacement of the computationally expensive controlled QAE routine with individually controlled state preparations V_ψ according to Eq. (45) for every possible cost $c(x)$.

Second, since the costs are manually set via the lookup table, we use the normalized cost $\tilde{c}(x)$, reducing the required number of phase qubits k due to its larger magnitude compared to the original cost $c(x)$ defined in Eq. (41).

The best achievable performance for QuSO corresponds to standard QAOA with the cost Hamiltonian H_C in Eq. (11). Thus, we benchmark QuSO results for different errors δ against QAOA simulations. For these simulations, the QAOA circuit parameters were initialized to $\gamma_i = \beta_i = 0.5$, and we varied the circuit depth from $p = 1$ to $p = 5$. For minimization, we used a gradient-descent optimizer with momentum which stopped once the cost improvement fell below a threshold of 1×10^{-5} . The resulting costs per iteration are shown in Fig. 10(a).

A typical performance metric in QAOA studies is the approximation ratio [22]

$$r = \frac{c_{\text{QAOA}}}{c_{\text{opt}}}, \quad (47)$$

where c_{QAOA} is the minimum cost obtained by QAOA, and c_{opt} is the global optimal cost. Consequently, $r = 1$ indicates that QAOA has found the optimal solution. Fig. 10(b) shows the approximation ratio of QuSO at various depths p and errors δ . For $\delta > 0$, we evaluated QuSO circuits using the optimal variational parameters $(\gamma_{\text{opt}}, \beta_{\text{opt}})$ obtained from standard QAOA simulations, whereas the results for $\delta = 0$ correspond to QAOA simulations. As expected, the approximation ratio of QAOA decreases with increasing depth approaching $r = 1$ asymptotically. While the QuSO results with $\delta = 2^{-2}$ show a completely different behavior, we can restore the QAOA-like behavior by further reducing δ .

Similar trends emerge in the $p = 1$ cost landscape plots in Fig. 11, visualizing the dependence of the objective

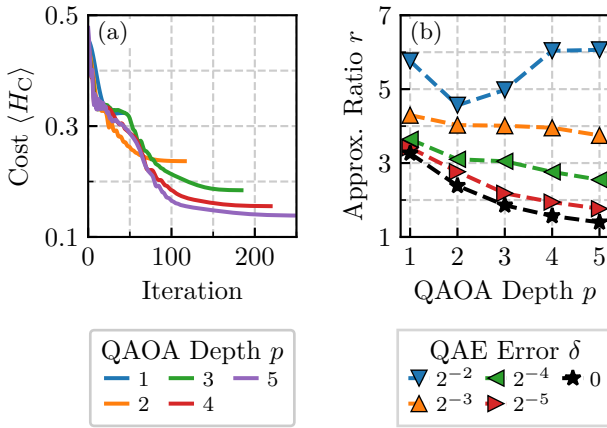


FIG. 10. (a) Costs per iteration for QAOA simulations across several depths. (b) Approximation ratio r for QuSO algorithm across depths p and errors δ .

function on the parameters γ and β . While the cost landscape with $\delta = 2^{-2}$ differs significantly from the ideal QAOA landscape ($\delta = 0$), the cost landscapes gradually converge toward the ideal behavior as δ decreases.

Finally, Fig. 12 illustrates the probability distributions after applying QuSO with depth $p = 5$. The bitstrings on the horizontal axis are ordered according to their respective costs, with optimal solutions positioned on the left and suboptimal solutions on the right. The QAOA circuit ($\delta = 0$) effectively amplifies the optimal amplitudes on the left. As observed previously, the QuSO results approach the QAOA result as δ decreases. Interestingly, at higher inaccuracies ($\delta = 2^{-2}$ and $\delta = 2^{-3}$), the probabilities of suboptimal solutions are also slightly amplified. This undesired amplification occurs due to the periodicity introduced by encoding the costs into the phase register in binary form, placing minimal cost values directly next to maximal ones. Consequently, when δ is too large, QuSO struggles to distinguish between optimal and suboptimal solutions. Fortunately, this effect is negligible once δ is sufficiently small.

Additionally, Fig. 12 shows the cooling system configurations corresponding to the five optimal bitstrings identified by the algorithm. Because our simplified cost function focuses solely on minimizing the battery temperature T_0 , it neglects thermal interactions in other parts of the system. As a result, in the optimal cooling system only the battery is connected to both coolers, and the engine, which produces most of the heat, is isolated. Although the algorithm successfully minimized the objective function, this is of course not a practically valid solution. Hence, a more sophisticated cost function is required for realistic systems.

V. CONCLUSION AND OUTLOOK

In this paper, we successfully demonstrated the QuSO algorithm on a simplified toy model of a cooling system inspired by automotive thermal management. By integrating quantum algorithms, including QAOA, LCU, QSVT, QAE, and QPA, we provided an end-to-end quantum algorithm capable of simulating and optimizing the cooling system.

Although our demonstration illustrates the capabilities of QuSO, it is important to emphasize that the considered scenario represents a highly simplified toy problem. Specifically, if the primary objective were to evaluate and minimize a single component of the solution vector (e.g., the battery temperature), solving just one equation would suffice instead of an entire system of equations. However, as previously mentioned, realistic applications would require more sophisticated cost functions that consider multiple or even all entries in the solution vector.

Moreover, our analysis indicates that the cooling system optimization problem, as presented, does not yield an exponential speedup in N . In particular, each QuSO iteration scales as $\mathcal{O}(N \log N)$, whereas the conjugate gradient method scales as $\mathcal{O}(N\sqrt{\kappa})$, and more general linear system solvers scale as $\mathcal{O}(N^3)$ [55]. Consequently, QuSO matches or outperforms classical methods in terms of asymptotic complexity, potentially offering a polynomial speedup for this problem. Achieving an exponential quantum speedup would require that the following subroutines or parameters scale at most logarithmically with N : the block-encoding of the problem matrix, the state preparation V_B , the condition number κ , the number of phase qubits k , and the number of QAOA iterations needed for convergence.

Since QAOA is inherently variational, our complexity analysis addresses only a single iteration of the optimization algorithm. Estimating the total number of iterations needed for convergence to the optimal solution is typically not feasible. Consequently, embedding the presented QuSO methodology into fault-tolerant quantum optimization frameworks, such as those leveraging Grover-based methods [56–59], could lead to provable quadratic advantages for the overall optimization procedure. Additionally, such fault-tolerant strategies mitigate common issues associated with variational quantum algorithms, such as barren plateaus.

Another promising direction is enhancing the QSVT subroutine through the adaptation of generalized Quantum Signal Processing [60], potentially reducing circuit depth significantly by utilizing general qubit rotations instead of only Z -rotations.

In conclusion, our demonstration highlights both the potential and limitations of QuSO. By explicitly analyzing the complexities of each quantum subroutine for a concrete example, this work sets the foundation for future research in quantum algorithms for

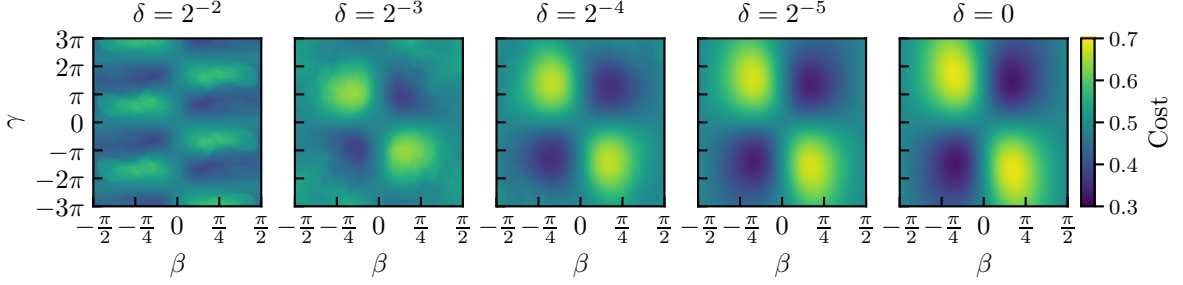


FIG. 11. Cost landscapes of the QuSO cost function at depth $p = 1$ for various accuracy levels δ .

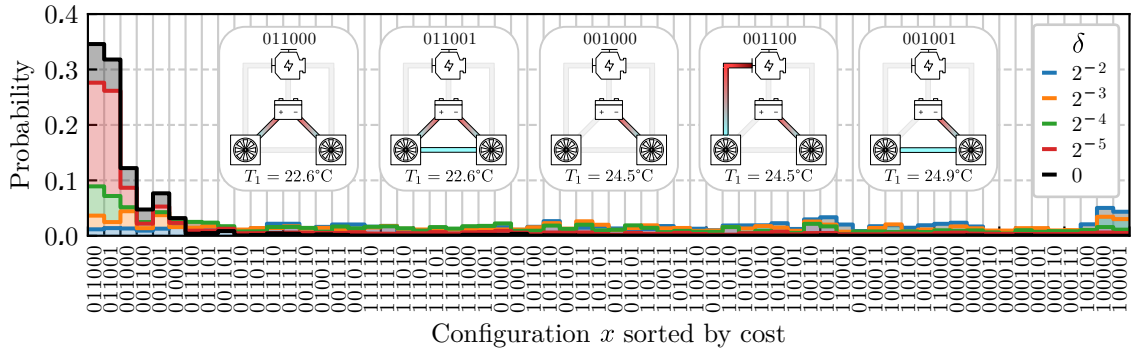


FIG. 12. Probability distributions obtained after optimization with QuSO at circuit depth $p = 5$ for various errors δ . Bitstrings are sorted by ascending cost (optimal solutions on the left). Insets depict the cooling system configurations corresponding to the five optimal bitstrings identified by the algorithm.

classical numerical simulations and simulation-based optimization.

ACKNOWLEDGMENTS

We acknowledge the support of the BMW Group and thank J. Stein for valuable insights and discussions. Additionally, we thank T. Stollenwerk and F. K. Wilhelm for ongoing support and constructive feedback. L. Müller is partly funded by the German Ministry for Economic Affairs and Energy (BMWE) in the project QCHALLenge under Grant 01MQ22008D.

Appendix A: Modeling the Cooling System

1. Derivation of the Linear System

As introduced in Section II, our cooling system considers only heat conduction. Thus, the heat transfer rate between two nodes i and j is given by

$$\dot{Q}_{ij} = \frac{T_i - T_j}{R_{ij}}. \quad (\text{A1})$$

Exemplarily, we consider the fully connected graph of Fig. 1(b) with $N = 4$ nodes. Since energy is conserved, the heat going in and out a node must be equal

$$\dot{Q}_0 + \frac{T_{\text{env}} - T_0}{R_{\text{env}}} = x_{01}\dot{Q}_{01} + x_{02}\dot{Q}_{02} + x_{03}\dot{Q}_{03} \quad (\text{A2})$$

$$\dot{Q}_1 + \frac{T_{\text{env}} - T_1}{R_{\text{env}}} + x_{01}\dot{Q}_{01} = x_{12}\dot{Q}_{12} + x_{13}\dot{Q}_{13} \quad (\text{A3})$$

$$\dot{Q}_2 + \frac{T_{\text{env}} - T_2}{R_{\text{env}}} + x_{02}\dot{Q}_{02} + x_{12}\dot{Q}_{12} = x_{23}\dot{Q}_{23} \quad (\text{A4})$$

$$\dot{Q}_3 + \frac{T_{\text{env}} - T_3}{R_{\text{env}}} + x_{03}\dot{Q}_{03} + x_{13}\dot{Q}_{13} + x_{23}\dot{Q}_{23} = 0. \quad (\text{A5})$$

Here, the binary variables x_{ij} determine if a connection and thus the heat flow from node i to j exists. In addition, every node is connected to the environment with temperature T_{env} and thermal resistance R_{env} . If we insert Eq. (A1) in the four equations above and sort the terms by the temperatures, we obtain the following linear system of equations

$$\begin{pmatrix}
\frac{1}{R_{\text{env}}} + \frac{x_{01}}{R_{01}} + \frac{x_{02}}{R_{02}} + \frac{x_{03}}{R_{03}} & -\frac{x_{01}}{R_{01}} & -\frac{x_{02}}{R_{02}} & -\frac{x_{03}}{R_{03}} \\
-\frac{x_{01}}{R_{01}} & \frac{1}{R_{\text{env}}} + \frac{x_{01}}{R_{01}} + \frac{x_{12}}{R_{12}} + \frac{x_{13}}{R_{13}} & -\frac{x_{12}}{R_{12}} & -\frac{x_{13}}{R_{13}} \\
-\frac{x_{02}}{R_{02}} & -\frac{x_{12}}{R_{12}} & \frac{1}{R_{\text{env}}} + \frac{x_{02}}{R_{02}} + \frac{x_{12}}{R_{12}} + \frac{x_{23}}{R_{23}} & -\frac{x_{23}}{R_{23}} \\
-\frac{x_{03}}{R_{03}} & -\frac{x_{13}}{R_{13}} & -\frac{x_{23}}{R_{23}} & \frac{1}{R_{\text{env}}} + \frac{x_{03}}{R_{03}} + \frac{x_{13}}{R_{13}} + \frac{x_{23}}{R_{23}}
\end{pmatrix}
\begin{pmatrix} T_0 \\ T_1 \\ T_2 \\ T_3 \end{pmatrix} \\
= \begin{pmatrix} \dot{Q}_0 + \frac{T_{\text{env}}}{R_{\text{env}}} \\ \dot{Q}_1 + \frac{T_{\text{env}}}{R_{\text{env}}} \\ \dot{Q}_2 + \frac{T_{\text{env}}}{R_{\text{env}}} \\ \dot{Q}_3 + \frac{T_{\text{env}}}{R_{\text{env}}} \end{pmatrix}. \quad (\text{A6})$$

To eliminate the constant term $T_{\text{env}}/R_{\text{env}}$ on the right-hand side of the equation, we reformulate the problem by solving for the shifted temperatures $\tilde{T}_i = T_i - T_{\text{env}}$ instead of T_i . This leads to the linear system presented in the main text (cf. Eq. (4)). The advantage of this transformation is that the vector \mathbf{B} becomes sparse if the system does not have many external heat sources. The thermal connection to the environment ensures that the matrix never becomes singular, even if all binary variables are set to zero.

For general systems with size N , the components of the linear system $\mathbf{A}\tilde{\mathbf{T}} = \mathbf{B}$ are given by

$$A_{ij} = \begin{cases} \frac{1}{R_{\text{env}}} + \sum_{(i,j) \in \mathbf{E}} \frac{x_{ij}}{R_{ij}} & \text{if } i = j, \\ -\frac{x_{ij}}{R_{ij}} & \text{if } i < j, \\ -\frac{x_{ji}}{R_{ji}} & \text{if } i > j. \end{cases} \quad (\text{A7})$$

$$\tilde{T}_i = T_i - T_{\text{env}} \quad (\text{A8})$$

$$B_i = \dot{Q}_i \quad (\text{A9})$$

2. Matrix Properties of the Linear System

The matrix \mathbf{A} , defined by Eq. (A7), is *real* and *symmetric* by construction. Furthermore, it is *strictly diagonally dominant*, as shown:

$$\sum_{j \neq i} |A_{ij}| < |A_{ii}| \quad (\text{A10})$$

$$\Leftrightarrow \sum_{(i,j) \in \mathbf{E}} \frac{x_{ij}}{R_{ij}} < \frac{1}{R_{\text{env}}} + \sum_{(i,j) \in \mathbf{E}} \frac{x_{ij}}{R_{ij}} \quad (\text{A11})$$

$$\Leftrightarrow 0 < \frac{1}{R_{\text{env}}}, \quad (\text{A12})$$

with $A_{ii} > 0$ since all resistances $R_{ij} > 0$. This property guarantees that \mathbf{A} is *positive definite* ($\mathbf{A} > 0$), implying that its eigenvalues λ_i are positive and correspond directly to its singular values ($\sigma_i = \lambda_i$).

The condition number of \mathbf{A} is defined as:

$$\kappa = \frac{\sigma_{\max}}{\sigma_{\min}} = \frac{\lambda_{\max}}{\lambda_{\min}}, \quad (\text{A13})$$

where λ_{\max} and λ_{\min} denote the largest and smallest eigenvalues, respectively.

To bound the eigenvalues, we apply the Gershgorin circle theorem [61], which gives:

$$|\lambda_i - A_{ii}| \leq \sum_{j \neq i} |A_{ij}|. \quad (\text{A14})$$

This leads to:

$$\lambda_{\min} \geq \min_i \left(A_{ii} - \sum_{j \neq i} |A_{ij}| \right), \quad (\text{A15})$$

$$\lambda_{\max} \leq \max_i \left(A_{ii} + \sum_{j \neq i} |A_{ij}| \right). \quad (\text{A16})$$

Substituting the matrix definition from Eq. (A7), we find:

$$\lambda_{\min} \geq \frac{1}{R_{\text{env}}}, \quad (\text{A17})$$

$$\lambda_{\max} \leq \frac{1}{R_{\text{env}}} + 2 \max_i \left(\sum_{(i,j) \in \mathbf{E}} \frac{x_{ij}}{R_{ij}} \right), \quad (\text{A18})$$

$$\leq \frac{1}{R_{\text{env}}} + 2 \frac{d_{\max}}{R_{\min}}, \quad (\text{A19})$$

where d_{\max} is the maximum degree of the graph (corresponding to the maximum number of connections of a component), and R_{\min} is the smallest resistance value in the system. Consequently, the condition number satisfies:

$$\kappa \leq 1 + 2d_{\max} \frac{R_{\text{env}}}{R_{\min}}. \quad (\text{A20})$$

Thus, the asymptotic scaling of the condition number is $\kappa = \mathcal{O}(d_{\max} R_{\text{env}} / R_{\min})$. This result is valid for every matrix $\mathbf{A}(x)$ regardless of the configuration x .

Appendix B: Agreement of Linear System and OpenModelica Solutions

To validate our modeling of the cooling system, we compare the results of the linear system in Eq. (A6) with

simulations within OpenModelica [34]. OpenModelica is an open-source modeling and simulation environment. Fig. 13 shows the graphical representation of the model with four nodes.

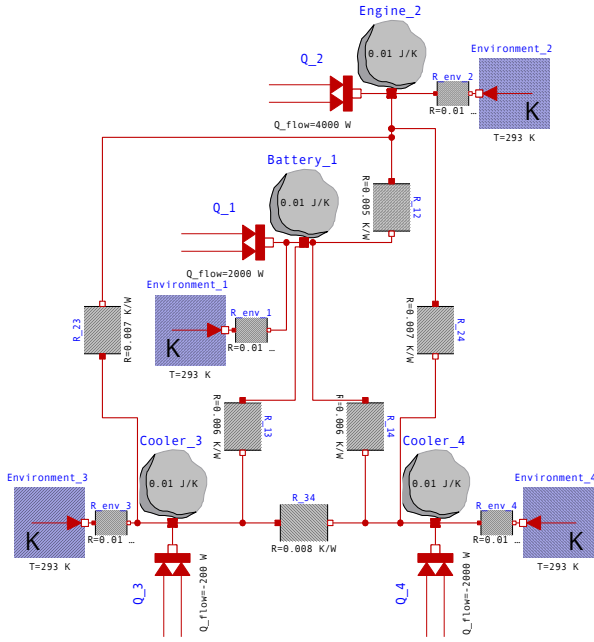


FIG. 13. Visualization of the cooling system model within OpenModelica.

Each component is represented by a heat capacitor with arbitrarily chosen thermal capacity 1 J/K . Additionally, the heat capacitor is connected to a heat source with fixed heat transfer rate \dot{Q}_i and to a thermal reservoir with temperature T_{env} via a thermal resistor with R_{env} . All capacitors are connected by the corresponding thermal resistors R_{ij} . To compare the models, we fix the system parameters as written in Table II. The simulation results for all system configurations using both models are shown in Fig. 14 and all temperatures \tilde{T}_i match perfectly. Consequently, our model of a simplified cooling system is valid.

Appendix C: QuSO Cost Layer

The QAOA cost layer is implemented in QuSO as

$$U_C(\gamma) \equiv \text{QAE}^\dagger \text{QPA}(\gamma) \text{QAE}. \quad (\text{C1})$$

As defined in Eq. (10), the cost layer modifies the phase associated with each configuration x in the c-register by incorporating both the cost $c(x)$ and the variational parameter γ . As explained in the main text, this operation requires additional registers, such as the phase register p and those required for the LCU block-encoding and QSVD (q , ℓ , f , ℓ' , and d). In the ideal case where the p -register has enough qubits to accurately represent

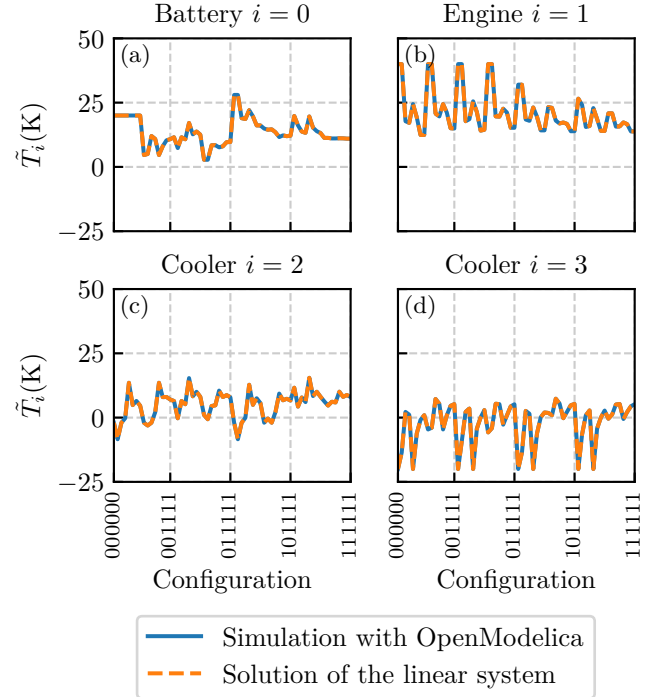


FIG. 14. Comparison of simulation results using our linear system and the OpenModelica model. The temperature $\tilde{T}_i = T_i - T_{\text{env}}$ is displayed for each configuration for (a) the battery, (b) the engine, and the two coolers in (c) and (d).

the phase $\theta = \arcsin(c(x))/\pi$, these additional registers are uncomputed after applying the cost layer

$$U_C(\gamma) |x\rangle_c |0\rangle_p |0\rangle = |x\rangle_c \underbrace{e^{-i\gamma c(x)} |0\rangle_p |0\rangle}_{=|\psi_{\text{ideal}}\rangle}. \quad (\text{C2})$$

In the following, we show that $|\psi_{\text{ideal}}\rangle$ has the form displayed in Eq. (C2). The QAE routine, which includes controlled gates on the c -register, computes the cost $c(x)$ and stores the corresponding phase θ in the p -register

$$\text{QAE} |0\rangle_{\text{p}} |0\rangle = c_+ |\theta\rangle_{\text{p}} |\psi_+\rangle + c_- |1-\theta\rangle_{\text{p}} |\psi_-\rangle. \quad (\text{C3})$$

Since the Grover operator G in Eq.(30) has two eigenvalues $\lambda_{\pm} = e^{\pm i 2\pi\theta}$, it effectively encodes both phases $\pm\theta$ in the p-register. In the binary fraction representation, the negative phase $-\theta$ is expressed as $1 - \theta$. The amplitudes c_{\pm} have the form

$$c_{\pm} = \mp \frac{i}{\sqrt{2}} e^{\mp i\pi\theta}. \quad (\text{C4})$$

The QAE operation is followed by QPA(γ) to add the

term $-i\gamma c(x)$ to the phase

$$\begin{aligned} & \text{QPA}(\gamma) \text{QAE} |0\rangle_p |0\rangle \\ &= c_+ \underbrace{e^{-i\gamma \sin(\pi\theta)}}_{=e^{-i\gamma c(x)}} |\theta\rangle_p |\psi_+ \rangle \\ &+ c_- \underbrace{e^{-i\gamma \sin(\pi(1-\theta))}}_{=e^{-i\gamma c(x)}} |1-\theta\rangle_p |\psi_- \rangle \\ &= e^{-i\gamma c(x)} \left(c_+ |\theta\rangle_p |\psi_+ \rangle + c_- |1-\theta\rangle_p |\psi_- \rangle \right). \end{aligned} \quad (\text{C5})$$

Finally, QAE^\dagger uncomputes all registers besides the outer c-register

$$\begin{aligned} \text{QAE}^\dagger \text{QPA}(\gamma) \text{QAE} |0\rangle_p |0\rangle &= e^{-i\gamma c(x)} |0\rangle_p |0\rangle \\ &= |\psi_{\text{ideal}}\rangle. \end{aligned} \quad (\text{C6})$$

In the general case where the p-register contains k qubits, the QAE routine computes the phase θ with a finite error of $\delta = 2^{-k}$. Consequently, the auxiliary registers are not entirely uncomputed, and the cost layer produces

$$U_C(\gamma) |x\rangle_c |0\rangle_p |0\rangle = |x\rangle_c |\psi_{\text{general}}\rangle. \quad (\text{C7})$$

We now derive the exact form of $|\psi_{\text{general}}\rangle$. Due to the error δ , the QAE operation does not yield a single state in the p-register for $|\psi_{\pm}\rangle$, respectively. Instead, it creates a superposition of states

$$\text{QAE} |0\rangle_p |0\rangle = \sum_{j=0}^{2^k-1} c_+ \alpha_+(j) |j\rangle_p |\psi_+ \rangle + c_- \alpha_-(j) |j\rangle_p |\psi_- \rangle. \quad (\text{C8})$$

Here, $\alpha_{\pm}(j)$ are the QPE amplitudes for $\pm\theta$ and are given by

$$\alpha_{\pm}(j) = \frac{1}{2^k} \sum_{l=0}^{2^k-1} e^{-i2\pi l(2^{-k}j \mp \theta)}. \quad (\text{C9})$$

The subsequent QPA(γ) operation yields

$$\begin{aligned} & \text{QPA}(\gamma) \text{QAE} |0\rangle_p |0\rangle \\ &= \sum_{j=0}^{2^k-1} c_+ \alpha_+(j) e^{-i\gamma \sin(\pi 2^{-k}j)} |j\rangle_p |\psi_+ \rangle \\ &+ c_- \alpha_-(j) e^{-i\gamma \sin(\pi 2^{-k}j)} |j\rangle_p |\psi_- \rangle \\ &= e^{-i\gamma c(x)} \left[\sum_{j=0}^{2^k-1} c_+ \alpha_+(j) |j\rangle_p |\psi_+ \rangle + c_- \alpha_-(j) |j\rangle_p |\psi_- \rangle \right] \\ &+ \sum_{j=0}^{2^k-1} c_+ \beta(j) \alpha_+(j) |j\rangle_p |\psi_+ \rangle + c_- \beta(j) \alpha_-(j) |j\rangle_p |\psi_- \rangle, \end{aligned} \quad (\text{C10})$$

where we have introduced the term

$$\beta(j) = e^{-i\gamma \sin(\pi 2^{-k}j)} - e^{-i\gamma \sin(\pi\theta)}. \quad (\text{C11})$$

The uncomputing step QAE^\dagger leads to

$$\begin{aligned} & \text{QAE}^\dagger \text{QPA}(\gamma) \text{QAE} |0\rangle_p |0\rangle \\ &= e^{-i\gamma c(x)} |0\rangle_p |0\rangle \\ &+ \text{QAE}^\dagger \sum_{j=0}^{2^k-1} c_+ \beta(j) \alpha_+(j) |j\rangle_p |\psi_+ \rangle \\ &+ c_- \beta(j) \alpha_-(j) |j\rangle_p |\psi_- \rangle \\ &= |\psi_{\text{general}}\rangle. \end{aligned} \quad (\text{C12})$$

We can use this expression to find an upper bound for the squared distance between the ideal and general outcome

$$\begin{aligned} & ||\psi_{\text{ideal}}\rangle - |\psi_{\text{general}}\rangle||^2 \\ &= \left| \sum_{j=0}^{2^k-1} c_+ \beta(j) \alpha_+(j) |j\rangle_p |\psi_+ \rangle + c_- \beta(j) \alpha_-(j) |j\rangle_p |\psi_- \rangle \right|^2 \\ &= \frac{1}{2} \sum_{j=0}^{2^k-1} |\beta(j)|^2 |\alpha_+(j)|^2 + |\beta(j)|^2 |\alpha_-(j)|^2 \end{aligned} \quad (\text{C13})$$

Similarly as in Ref. [42] (p. 224), we can bound $|\alpha_{\pm}(j)|^2$ using the geometric series and the inequalities $|1 - e^{i\varphi_1}| \leq 2$ and $|1 - e^{i\varphi_2}| \geq 2|\varphi_2|/\pi$ for $-\pi \leq \varphi_2 \leq \pi$:

$$\begin{aligned} |\alpha_+(j)|^2 &= \left| \frac{1}{2^k} \sum_{l=0}^{2^k-1} e^{-i2\pi l(2^{-k}j - \theta)} \right|^2 \\ &= \left| \frac{1}{2^k} \frac{1 - e^{-i2\pi(2^{-k}j - \theta)2^k}}{1 - e^{-i2\pi(2^{-k}j - \theta)}} \right|^2 \\ &\leq \frac{1}{2^{2k}} \frac{4}{|1 - e^{-i2\pi(2^{-k}j - \theta)}|^2} \\ &= \frac{1}{2^{2k+2}} \frac{1}{(2^{-k}j - \theta)^2}. \end{aligned} \quad (\text{C14})$$

The same procedure leads to

$$|\alpha_-(j)|^2 \leq \frac{1}{2^{2k+2}} \frac{1}{(2^{-k}j - 1 + \theta)^2}. \quad (\text{C15})$$

By elementary calculus, we find the bounds

$$\begin{aligned} |\beta(j)|^2 &= \left| e^{-i\gamma \sin(\pi 2^{-k}j)} - e^{-i\gamma \sin(\pi\theta)} \right|^2 \\ &\leq |\gamma \sin(\pi 2^{-k}j) - \gamma \sin(\pi\theta)|^2 \\ &\leq \gamma^2 \pi^2 (2^{-k}j - \theta)^2 \end{aligned} \quad (\text{C16})$$

and

$$\begin{aligned} |\beta(j)|^2 &= \left| e^{-i\gamma \sin(\pi 2^{-k}j)} - e^{-i\gamma \sin(\pi(1-\theta))} \right|^2 \\ &\leq \gamma^2 \pi^2 (2^{-k}j - 1 + \theta)^2. \end{aligned} \quad (\text{C17})$$

Combining all inequalities from Eqs. (C14), (C15), (C16),

(C17) and our expression in Eq. (C13), we obtain

$$\begin{aligned}
& |\langle \psi_{\text{ideal}} \rangle - \langle \psi_{\text{general}} \rangle|^2 \\
&= \frac{1}{2} \sum_{j=0}^{2^k-1} |\beta(j)|^2 |\alpha_+(j)|^2 + |\beta(j)|^2 |\alpha_-(j)|^2 \\
&\leq \frac{1}{2} \sum_{j=0}^{2^k-1} \gamma^2 \pi^2 (2^{-k}j - \theta)^2 \frac{1}{2^{2k+2}} \frac{1}{(2^{-k}j - \theta)^2} \\
&\quad + \gamma^2 \pi^2 (2^{-k}j - 1 + \theta)^2 \frac{1}{2^{2k+2}} \frac{1}{(2^{-k}j - 1 + \theta)^2} \\
&= \frac{\gamma^2 \pi^2}{2^{k+2}}.
\end{aligned} \tag{C18}$$

Consequently, we have shown that the squared distance between the ideal state and the general state after a single cost layer scales as

$$|\langle \psi_{\text{ideal}} \rangle - \langle \psi_{\text{general}} \rangle|^2 = \mathcal{O}(2^{-k}) = \mathcal{O}(\delta). \tag{C19}$$

[1] C. A. Riofrío, J. Klepsch, J. R. Finžgar, F. Kiwit, L. Hölscher, M. Erdmann, L. Müller, C. Kumar, Y. A. Berrada, and A. Luckow, Quantum Computing for Automotive Applications (2024), arXiv:2409.14183 [quant-ph].

[2] A. M. Dalzell, S. McArdle, M. Berta, P. Bienias, C.-F. Chen, A. Gilyén, C. T. Hann, M. J. Kastoryano, E. T. Khabiboulline, A. Kubica, G. Salton, S. Wang, and F. G. S. L. Brandão, Quantum algorithms: A survey of applications and end-to-end complexities (2023), arXiv:2310.03011 [quant-ph].

[3] S. Jin and N. Liu, Analog quantum simulation of partial differential equations, *Quantum Science and Technology* **9**, 035047 (2024).

[4] O. Kyriienko, A. E. Paine, and V. E. Elfving, Solving nonlinear differential equations with differentiable quantum circuits, *Physical Review A* **103**, 052416 (2021).

[5] M. Lubasch, J. Joo, P. Moinier, M. Kiffner, and D. Jaksch, Variational quantum algorithms for nonlinear problems, *Physical Review A* **101**, 010301 (2020).

[6] D. Jaksch, P. Givi, A. J. Daley, and T. Rung, Variational Quantum Algorithms for Computational Fluid Dynamics, *AIAA Journal* **61**, 1885 (2023).

[7] R. Demirdjian, D. Gunlycke, C. A. Reynolds, J. D. Doyle, and S. Tafur, Variational quantum solutions to the advection–diffusion equation for applications in fluid dynamics, *Quantum Information Processing* **21**, 322 (2022).

[8] D. W. Berry, High-order quantum algorithm for solving linear differential equations, *Journal of Physics A: Mathematical and Theoretical* **47**, 105301 (2014).

[9] D. W. Berry, A. M. Childs, A. Ostrander, and G. Wang, Quantum Algorithm for Linear Differential Equations with Exponentially Improved Dependence on Precision, *Communications in Mathematical Physics* **356**, 1057 (2017).

[10] A. Montanaro and S. Pallister, Quantum algorithms and the finite element method, *Physical Review A* **93**, 032324 (2016).

[11] A. W. Harrow, A. Hassidim, and S. Lloyd, Quantum Algorithm for Linear Systems of Equations, *Physical Review Letters* **103**, 150502 (2009).

[12] A. M. Childs, R. Kothari, and R. D. Somma, Quantum Algorithm for Systems of Linear Equations with Exponentially Improved Dependence on Precision, *SIAM Journal on Computing* **46**, 1920 (2017).

[13] A. Gilyén, Y. Su, G. H. Low, and N. Wiebe, Quantum singular value transformation and beyond: exponential improvements for quantum matrix arithmetics, in *Proceedings of the 51st Annual ACM SIGACT Symposium on Theory of Computing* (ACM, Phoenix AZ USA, 2019) pp. 193–204.

[14] J. M. Martyn, Z. M. Rossi, A. K. Tan, and I. L. Chuang, Grand Unification of Quantum Algorithms, *PRX Quantum* **2**, 040203 (2021).

[15] M. E. S. Morales, L. Pira, P. Schleich, K. Koor, P. C. S. Costa, D. An, A. Aspuru-Guzik, L. Lin, P. Rebentrost, and D. W. Berry, Quantum Linear System Solvers: A Survey of Algorithms and Applications (2025), arXiv:2411.02522 [quant-ph].

[16] O. Axelsson and V. A. Barker, *Finite Element Solution of Boundary Value Problems: Theory and Computation* (Society for Industrial and Applied Mathematics, 2001).

[17] R. H. Landau, *A survey of computational physics: introductory computational science* (Princeton University Press, Princeton, 2008).

[18] S. Aaronson, Read the fine print, *Nature Physics* **11**, 291 (2015).

[19] J. Stein, L. Müller, L. Hölscher, G. Chnitidis, J. Jojo, A. Farea, M. S. Çelebi, D. Bucher, J. Wulf,

D. Fischer, P. Altmann, C. Linnhoff-Popien, and S. Feld, Exponential Quantum Speedup for Simulation-Based Optimization Applications (2024), arXiv:2305.08482 [quant-ph].

[20] L.-F. Wang and L.-Y. Shi, Simulation Optimization: A Review on Theory and Applications, *Acta Automatica Sinica* **39**, 1957 (2013).

[21] A.-T. Nguyen, S. Reiter, and P. Rigo, A review on simulation-based optimization methods applied to building performance analysis, *Applied Energy* **113**, 1043 (2014).

[22] E. Farhi, J. Goldstone, and S. Gutmann, A Quantum Approximate Optimization Algorithm (2014), arXiv:1411.4028 [quant-ph].

[23] S. Hadfield, Z. Wang, B. O’Gorman, E. G. Rieffel, D. Venturelli, and R. Biswas, From the Quantum Approximate Optimization Algorithm to a Quantum Alternating Operator Ansatz, *Algorithms* **12**, 34 (2019), arXiv:1709.03489 [quant-ph].

[24] C. Sünderhauf, E. Campbell, and J. Camps, Block-encoding structured matrices for data input in quantum computing, *Quantum* **8**, 1226 (2024).

[25] D. Camps, L. Lin, R. Van Beeumen, and C. Yang, Explicit Quantum Circuits for Block Encodings of Certain Sparse Matrices, *SIAM Journal on Matrix Analysis and Applications* **45**, 801 (2024).

[26] A. M. Childs and N. Wiebe, Hamiltonian Simulation Using Linear Combinations of Unitary Operations, *Quantum Information and Computation* **12**, 10.26421/QIC12.11-12 (2012).

[27] G. Brassard, P. Høyer, M. Mosca, and A. Tapp, Quantum amplitude amplification and estimation, in *Contemporary Mathematics*, Vol. 305, edited by S. J. Lomonaco and H. E. Brandt (American Mathematical Society, Providence, Rhode Island, 2002) pp. 53–74.

[28] Y. Sato, R. Kondo, S. Koide, and S. Kajita, Quantum topology optimization of ground structures using noisy intermediate-scale quantum devices (2022), arXiv:2207.09181 [quant-ph].

[29] Z. Ye, X. Qian, and W. Pan, Quantum Topology Optimization via Quantum Annealing (2023), arXiv:2301.11531 [math].

[30] J. H. Lienhard, V and J. H. Lienhard, IV, *A Heat Transfer Textbook*, 6th ed. (Phlogiston Press, Cambridge, MA, 2024).

[31] S. Lloyd, G. D. Palma, C. Gokler, B. Kiani, Z.-W. Liu, M. Marvian, F. Tennie, and T. Palmer, Quantum algorithm for nonlinear differential equations (2020), arXiv:2011.06571 [quant-ph].

[32] J.-P. Liu, H. Ø. Kolden, H. K. Krovi, N. F. Loureiro, K. Trivisa, and A. M. Childs, Efficient quantum algorithm for dissipative nonlinear differential equations, *Proceedings of the National Academy of Sciences* **118**, 10.1073/pnas.2026805118 (2021).

[33] S. Jin and N. Liu, Quantum algorithms for computing observables of nonlinear partial differential equations (2022), arXiv:2202.07834 [quant-ph].

[34] P. Fritzson, A. Pop, K. Abdelhak, A. Ashgar, B. Bachmann, W. Braun, D. Bouskela, R. Braun, L. Buffoni, F. Casella, R. Castro, R. Franke, D. Fritzson, M. Gebremedhin, A. Heuermann, B. Lie, A. Mengist, L. Mikelsons, K. Moudgalya, L. Ochel, A. Palanisamy, V. Ruge, W. Schamai, M. Sjölund, B. Thiele, J. Timmerholm, and P. Östlund, The OpenModelica Integrated Environment for Modeling, Simulation, and Model-Based Development, *Modeling, Identification and Control* **41**, 241 (2020).

[35] M. Born and V. Fock, Beweis des Adiabatensatzes, *Zeitschrift für Physik* **51**, 165 (1928).

[36] M. Suzuki, Decomposition formulas of exponential operators and Lie exponentials with some applications to quantum mechanics and statistical physics, *Journal of Mathematical Physics* **26**, 601 (1985).

[37] J. Huyghebaert and H. D. Raedt, Product formula methods for time-dependent Schrödinger problems, *Journal of Physics A: Mathematical and General* **23**, 5777 (1990).

[38] A. Barenco, C. H. Bennett, R. Cleve, D. P. DiVincenzo, N. Margolus, P. Shor, T. Sleator, J. A. Smolin, and H. Weinfurter, Elementary gates for quantum computation, *Physical Review A* **52**, 3457 (1995).

[39] X.-M. Zhang, T. Li, and X. Yuan, Quantum State Preparation with Optimal Circuit Depth: Implementations and Applications, *Physical Review Letters* **129**, 230504 (2022).

[40] L. Grover and T. Rudolph, Creating superpositions that correspond to efficiently integrable probability distributions (2002), arXiv:quant-ph/0208112.

[41] M. Ozols, M. Roetteler, and J. Roland, Quantum rejection sampling, *ACM Transactions on Computation Theory* **5**, 1 (2013).

[42] M. A. Nielsen and I. L. Chuang, *Quantum Computation and Quantum Information: 10th Anniversary Edition*, 1st ed. (Cambridge University Press, 2012).

[43] L. K. Grover, A fast quantum mechanical algorithm for database search (1996), arXiv:quant-ph/9605043.

[44] G. H. Low and I. L. Chuang, Optimal Hamiltonian Simulation by Quantum Signal Processing, *Physical Review Letters* **118**, 010501 (2017).

[45] The QSVT operator in some literature includes an additional projector-controlled phase-shift operation. This introduces an extra phase angle ϕ_0 or ϕ_{d+1} , which is required to transition between different conventions of block-encoding.

[46] Y. Dong, X. Meng, K. B. Whaley, and L. Lin, Efficient phase-factor evaluation in quantum signal processing, *Physical Review A* **103**, 042419 (2021).

[47] In Ref.[14], the authors set $\mu = 1/\kappa$ under the assumption that the largest singular value $\sigma_{\max} = 1$. Since this is not true in general, we introduce μ to avoid confusion with the condition number κ .

[48] D. Ramacciotti, A. I. Lefterovici, and A. F. Rotundo, Simple quantum algorithm to efficiently prepare sparse states, *Physical Review A* **110**, 032609 (2024).

[49] G. Collins and N. A. D. System, *Fundamental Numerical Methods and Data Analysis* (George W. Collins, II, 2003).

[50] J. Welch, D. Greenbaum, S. Mostame, and A. Aspuru-Guzik, Efficient quantum circuits for diagonal unitaries without ancillas, *New Journal of Physics* **16**, 033040 (2014).

[51] S. M. Lim, C. E. Susa, and R. Cohen, Curve-Fitted QPE: Extending Quantum Phase Estimation Results for a Higher Precision using Classical Post-Processing (2024), arXiv:2409.15752 [quant-ph].

[52] F. G. Fuchs, K. O. Lye, H. M. Nilsen, A. J. Stasik, and G. Sartor, Constrained mixers for the quantum approximate optimization algorithm, *Algorithms* **15**, 202

(2022), arXiv:2203.06095 [quant-ph].

[53] L. Hölscher, Quantum Simulation-Based Optimization of a Cooling System.

[54] L. Hölscher, L. Müller, O. Samimi, and T. Danzig, Cooling System Optimization.

[55] G. H. Golub and C. F. Van Loan, *Matrix computations*, fourth edition ed., Johns Hopkins studies in the mathematical sciences (The Johns Hopkins University Press, Baltimore, 2013).

[56] C. Durr and P. Hoyer, A Quantum Algorithm for Finding the Minimum (1999), arXiv:quant-ph/9607014.

[57] D. Bulger, W. P. Baritompa, and G. R. Wood, Implementing Pure Adaptive Search with Grover's Quantum Algorithm, *Journal of Optimization Theory and Applications* **116**, 517 (2003).

[58] W. P. Baritompa, D. W. Bulger, and G. R. Wood, Grover's Quantum Algorithm Applied to Global Optimization, *SIAM Journal on Optimization* **15**, 1170 (2005).

[59] A. Gilliam, S. Woerner, and C. Gonciulea, Grover Adaptive Search for Constrained Polynomial Binary Optimization, *Quantum* **5**, 428 (2021).

[60] D. Motlagh and N. Wiebe, Generalized Quantum Signal Processing, *PRX Quantum* **5**, 020368 (2024).

[61] S. A. Gershgorin, Über die Abgrenzung der Eigenwerte einer Matrix., *Bulletin de l'Académie des Sciences de l'URSS. VII. Série* **1931**, 749 (1931).